Showcasing research from the group of Prof. Mizuki Tada at Nagoya University, Japan

In situ 3D X-ray imaging of water distribution in each layer of a membrane electrode assembly of a polymer electrolyte fuel cell

H. Matsui and M. Tada's group is working on the *in situ* visualization of functional materials at work by hard X-ray spectroimaging. This work investigates the 3D imaging of water distribution in each stacking layer of gas diffusion layers and membrane electrode assembly of a polymer electrolyte fuel cell. For the first time, the statistical analysis of the 3D image data sets elucidated physical–chemical trends, which supposed the interference of the electrochemical water production and drainage properties.

ROYAL SOCIETY OF CHEMISTRY

rsc.li/pccp

Registered charity number: 207890

PCCP Owner Societies

ROYAL SOCIETY
OF CHEMISTRY

COMMUNICATION

Check for updates

In situ 3D X-ray imaging of water distribution in each layer of a membrane electrode assembly of a polymer electrolyte fuel cell†

Hirosuke Matsui, [iD] ⋆[ab] Tomoro Ohta,[ab] Takahiro Nakamura,[a] Tomoya Uruga[c] and Mizuki Tada⋆[ab]

In situ 3D computed tomography imaging with statistical analysis successfully revealed the water accumulation and drainage characteristics in the stacked gas diffusion layers (GDLs) and membrane electrode assembly (MEA) of a polymer electrolyte fuel cell. Efficient water drainage at the interface between the cathode GDL and MEA was confirmed upon supplying oxygen to the cathode.

The management and drainage control of liquid water in polymer electrolyte fuel cells (PEFCs), which have stacked structures comprising a membrane electrode assembly (MEA) with a cathode catalyst layer, electrolyte, and an anode catalyst layer, gas diffusion layers (GDLs), and gas/fluid channels are essential for achieving stable and high volumetric power density.[1] The protons and electrons formed from the hydrogen fuel at the anode are transferred to the cathode, where they react with oxygen to generate water through the oxygen reduction reaction (ORR). The operation of a PEFC requires high humidity to maintain the proton conductivity of the polymer electrolyte membrane (PEM) in the MEA,[2–4] and humidified gases are thus supplied to both the anode and cathode. However, the resulting accumulation of water affects the electrochemical performance and drainage properties by impeding mass transport in the GDLs and gas/fluid channels, and the formation of liquid water can cause significant power loss and ultimately flooding of the PEFC.[5]

Simulations and material design to control hydration and water drainage inside PEFCs have been widely investigated in the field of fluid engineering,[6–9] but the multiple sites of water accumulation under PEFC working conditions made it difficult to characterize the spatiotemporal distribution of liquid water inside PEFCs comprising several components, such as gas/fluid channels, microporous-containing GDLs, and catalyst layers (CLs) of the MEA. Various attempts have been made to visualize water accumulation and transport in PEFCs using optical and spectroscopic techniques.[10–13] For instance, optical microscopy revealed the percolation, growth, and desorption of water droplets on the GDL surface and inside the gas/fluid channels.[14,15] Samples with small through holes in the GDL and MEA CL enabled observation of the hydration and mass transport within the internal structures.[16–18] However, it remains difficult to visualize the internal structures and water distributions at each layer of GDLs and MEA composed of organic compounds. In this regard, high-transmission probes such as neutrons[19,20] and X-rays[21–23] hold promise for the *in situ* and non-destructive imaging of liquid water accumulation in each component of PEFCs.

X-ray radiography/computed tomography (CT) techniques have been successfully applied to the 2D/3D imaging of liquid water in PEFCs.[24–26] Previous expertized works revealed the different distribution of liquid water to the support materials of catalyst layers,[27] the growth of liquid water droplets and the removal of water plugs in the fluid channel of operating PEFC,[28] the requirement of a microporous layer to decrease the liquid water at the interface of MEA CL and GDL, and so forth.[29] In addition, high-speed 4D neutron CT allowed quantitative analysis of the water distribution in a PEFC during operation, albeit with limited spatial resolution (the MEA and GDLs were observed as a single layer).[30] In other pioneering works, Büchi, Eller, and co-workers accomplished subsecond X-ray CT imaging by developing a bespoke PEFC for rapid rotary CT scanning.[31,32] A small capillary-like PEFC was used to monitor the transient behavior of water evolution and drainage in the GDLs toward the gas/fluid channels. However, the cell had a cylindrical shape of millimeter size, which is dissimilar to the structures of practically available PEFCs.

[a] Department of Chemistry, Graduate School of Science & Research Center for Materials Science (RCMS) & Integrated Research Consortium on Chemical Science (IRCCS) & Reaction Infography (R-ing) World Research Unit, Nagoya University, Furo, Chikusa, Nagoya, Aichi 464-8602, Japan. E-mail: matsui.hirosuke.x1@f.mail.nagoya-u.ac.jp, tada.mizuki.u6@f.mail.nagoya-u.ac.jp

[b] RIKEN SPring-8 Center, SPring-8, Koto, Sayo, Hyogo 679-5198, Japan

[c] Japan Synchrotron Radiation Research Center, SPring-8, Koto, Sayo, Hyogo 679-5198, Japan

† Electronic supplementary information (ESI) available: Experimental and analytical procedures, electrochemical experiments, other example of CT analysis. See DOI: https://doi.org/10.1039/d4cp00728j

Here, we report on the use of *in situ* CT imaging using hard X-rays for 3D quantitative imaging of the water distributions in the layered structures of a standard PEFC during operation. X-Ray imaging at 9 keV in a voxel resolution of 0.65 μm afforded sufficient contrast of the PEFC components, and the difference images calculated from the CT images recorded under wet and dry operating conditions successfully enabled 3D visualization of the water distributions in the PEFC under different operating conditions. The statistical analysis of the *in situ* CT images in each of the PEFC components for the first time elucidated physical–chemical trends, which supposed the interference of the electrochemical water production and drainage properties.

The *in situ* X-ray CT imaging was conducted at the BL36XU station of SPring-8 (Fig. S1(a), ESI†).[33] A commercially available MEA composed of a cathode catalyst layer, electrolyte, and an anode catalyst layer was used in an *in situ* XAFS cell (MEA size: 30 mm × 30 mm, Fig. S1(c), ESI†) to fabricate a PEFC customized for *in situ* CT measurements with an acceptable X-ray projection angle (θ) of ±80°. The PEFC containing the MEA was heated at 353 K and conditioned by 150 *I–V* cycles (Supplementary Methods and Fig. S1(b and c), ESI†). The electrochemical performance of the conditioned MEA was similar to that reported in our previous study (Fig. S2, ESI†).[25] To calculate 3D images of the water in the PEFC, we first performed measurements in the absence of conspicuous water accumulation (dry conditions: N$_2$ flow with a relative humidity (RH) of 64%) and recorded the CT data. Next, the PEFC was operated under wet conditions at 0.4 V. After the cell current had been steady for at least 15 min, both the inlet and outlet gas valves of the PEFC were closed to quench the reactions inside the MEA. After confirming that the cell current had fallen to zero due to the cessation of the fuel supply, limited-angle rotary CT scans were conducted with $\theta = \pm 80°$ (Fig. S3, ESI†), which is applicable for the 3D imaging of flat objects.[34] The CT measurements were performed for 32 s and the CT data sets exhibiting negligible changes in the water distribution during the measurements were used in the subsequent analysis.

The 3D volumetric images on the left side of Fig. 1(a) show the morphologies of the GDLs and the conditioned MEA CLs under dry conditions (N$_2$ flow to the cathode with RH = 64%). We compared the contrasts of the water signals obtained after collecting CT data at 9, 12, and 25 keV and found that 9 keV afforded the clearest images of the water inside the MEA. The pixel resolution was 0.65 μm in every sample dimension (*XYZ*), which was sufficient for identifying the layered structures of the MEA and GDLs. The corresponding 2D cross-sectional images
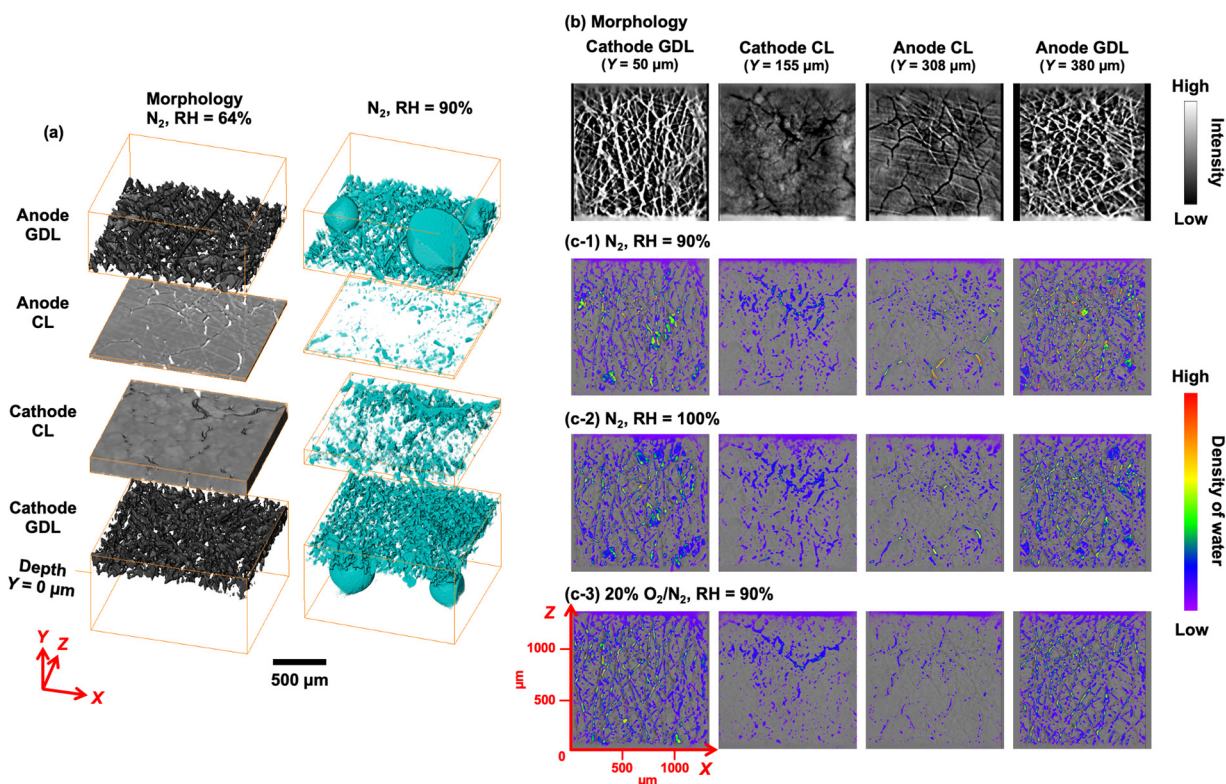

Fig. 1 (a) (left) 3D images showing the morphologies of the PEFC layers reconstructed from the *in situ* X-ray CT data recorded at 9 keV. The PEFC was operated in the absence of conspicuous water accumulation (dry conditions) by supplying N$_2$ with a relative humidity (RH) of 64% to the cathode. (right) Calculated 3D images of the water distributions on the MEA with GDLs, obtained by subtracting the image under dry conditions (RH = 64%) from the corresponding image under wet conditions (RH = 90%). 2D cross-sectional images of the (b) sample morphology and (c) water distribution at the center of each layer (cathode gas diffusion layer (GDL), *Y* = 50 μm; cathode catalyst layer (CL), *Y* = 155 μm; anode CL, *Y* = 308 μm; and anode GDL, *Y* = 380 μm). *Y* = 0 μm was defined as the depth of the cathode GDL surface. The PEFC was operated at 353 K at 0.4 V under the following cathode conditions: (1) N$_2$ flow with RH = 90%, (2) N$_2$ flow with RH = 100%, and (3) 20% O$_2$/N$_2$ flow with RH = 90%. For the results of additional batch experiments, see Fig. S5 (ESI†).

15116 | *Phys. Chem. Chem. Phys.*, 2024, **26**, 15115–15119

This journal is © the Owner Societies 2024

at the centers of the cathode GDL (Y = 50 μm), cathode CL (Y = 155 μm), anode CL (Y = 308 μm), and anode GDL (Y = 380 μm) are presented in Fig. 1(b). In this system, the GDLs were composed of laminated carbon fibers, which form micron-sized diffusion paths for the reaction gases and water, and this morphology was clearly observed in the CT images. By contrast, the CLs had a completely different morphology featuring numerous crack structures formed during the initial MEA preparation. These morphological differences were observed in the PEFC lateral dimension (Y) and agreed with the structures of the component materials revealed by scanning electron microscopy and our previous results,[35] indicating that the present CT imaging technique enabled successful visualization of the 3D structures in the PEFC.

The X-ray absorbance of water in the PEFC, whose contrast was estimated to be almost 6.7% of the average contrasts of the PEFC components (the MEA and GDLs), was calculated using the Beer–Lambert law for the CT data obtained from the same position under dry and wet operating conditions (for the details, see Supplementary Methods and Fig. S4, ESI†). A custom-made analysis program with six-dimensional affine transformation was employed to match the observed data by translation ($T_X T_Y T_Z$) and scaling ($S_X S_Y S_Z$), thus accounting for the swelling of the MEA in the presence of moisture. We confirmed that the intense signal contrast derived from the PEFC, which was approximately 15 times greater than the water

signal, was successfully eliminated and the values greater than that at the outside of the sample in the residual signal was identified and automatically detected as water, considering the signal-to-noise ratio of the imaging data.

The residual signals were overlaid on the 3D images (Fig. 1(a), right side) and 2D cross-sectional images (Fig. 1(c) and Fig. S5, ESI†). The water distributions clearly varied between the different layers of the GDLs and the MEA CLs. The GDLs exhibited far greater condensation of water compared with the MEA CLs, and water droplets were observed on the GDL surface that may have percolated from the GDLs. The cathode CL contained numerous cracks formed during the preparation process, and the water signal intensity was high in these regions. Fine spots corresponding to small water droplets were also observed in the body of the CL (Fig. 1(c) and Fig. S5, ESI†). We recorded *in situ* CT images at the same position under three sets of cathode operating conditions: (1) under N_2 flow without O_2 with RH = 90%, (2) under N_2 flow without O_2 with RH = 100%, and (3) under 20% O_2/N_2 flow with RH = 90%. Conditions (1) and (2) using a flow of humidified N_2 provided images of the water originating from the humidified gas, while condition (3) with the inclusion of O_2 gave images of the water derived from both the humidified gas and the ORR product.

The reconstructed 3D images were huge data sets containing a large amount of information about the quantity and spatial occupancy of the water in the MEA and GDLs (approximately 26
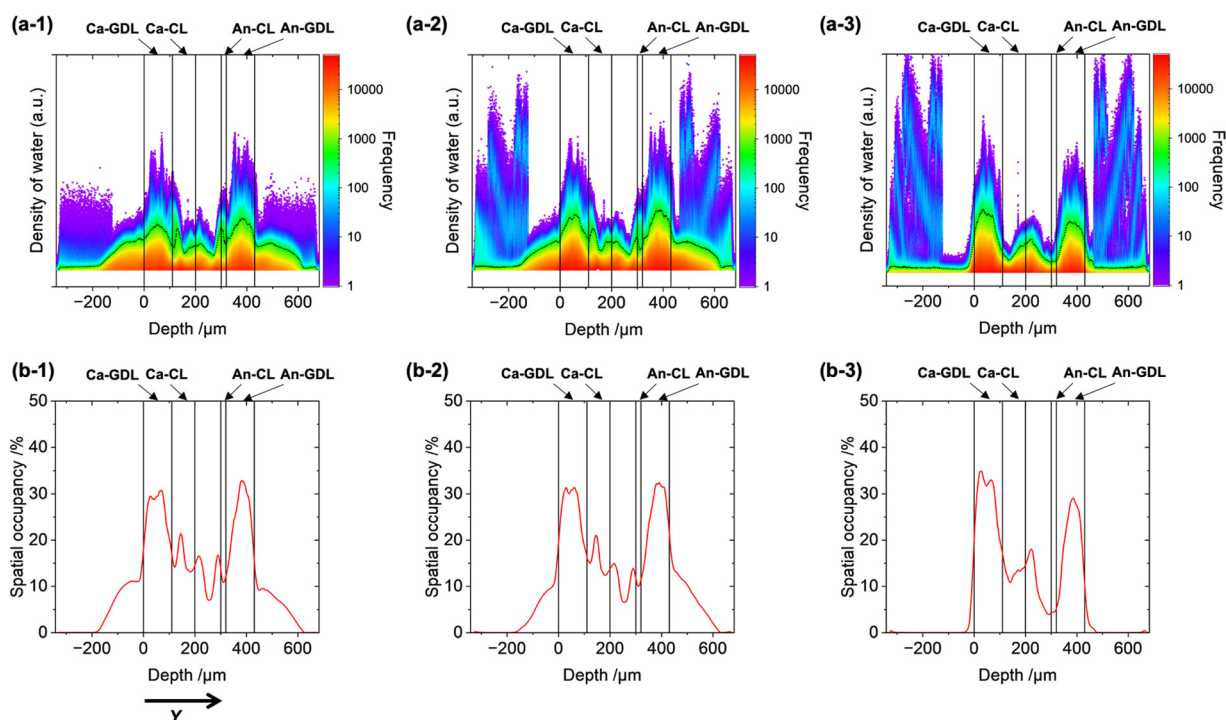

Fig. 2 (a) 2D histograms of the liquid water density with respect to sample depth (Y) for the PEFC during operation. The color of the 2D map represents the smoothed color density representation of the scatter plot based on the logarithmic kernel density estimation. (b) Rate of spatial occupancy of liquid water retained in the stacking geometry of the MEA with GDLs inside the PEFC. The spatial occupancy rate was estimated as the percentage of voxels where water was detected relative to the total voxels at each depth. The PEFC was operated under the following cathode conditions: (1) under N_2 flow with RH = 90%, (2) under N_2 flow with RH = 100%, and (3) under 20% O_2/N_2 flow with RH = 90%. For the results of additional batch experiments, see Fig. S6 (ESI†).

This journal is © the Owner Societies 2024

Phys. Chem. Chem. Phys., 2024, **26**, 15115–15119 | **15117**

million in-plane voxels (XZ) and 859 voxels in the depth direction (Y)). We analyzed the trends of the water distributions with respect to depth by using the statistical data obtained from the 3D imaging. The logarithmic kernel density estimation was used to prepare 2D histograms, where the vertical axis shows the frequency of voxels with a particular water density as a color map and the horizontal axis shows the depth (Y) (Fig. 2(a) and Fig. S6, ESI†). Depth profiles of the spatial occupancy of water (%), which was defined as the percentage of voxels where water was detected relative to all voxels in the image, were also plotted (Fig. 2(b)). $Y = 0$ μm was defined as the cathode GDL surface and the boundaries of each layer were determined from the CT images of the sample morphology.

The trends of the water density under the three sets of PEFC operating conditions revealed areas of water trapped in the PEFC membrane. Operation of the PEFC under condition (1) (under N_2 flow with RH = 90% at 0.4 V) revealed a wide variation of the water density in each layer (Fig. 2(a-1) and Fig. S6(a), ESI†). Water was also observed in the negative depth range, which was outside of the cathode GDL. Although the maximum water density in this region ($Y < -200$ μm) was relatively high, the spatial occupancy was rather limited (low frequency) (Fig. 2(b-1)), indicating that the CT imaging technique detected liquid water droplets drained from the GDL to the gas/fluid channels.

The water density distributions exhibited similar volcano-like shapes in the cathode GDL and anode GDL regions, suggesting that water accumulation was especially prominent at the centers of the GDLs, which may be attributable to the limited water-repellent effect. The spatial occupancy in the GDLs was approximately 30%, with the highest frequency in the set of PEFC samples (Fig. 2(b-1)). In the cathode CL, there was a large increase in the water density from the interface with the cathode GDL (Y = 110–150 μm), which may have resulted from the marked difference in porosities between the GDL and CL.[32]

Upon increasing the RH of the cathode gas (condition (2), under N_2 flow with RH = 100%), the shape of the 2D histogram inside the MEA CLs and GDLs was almost identical to that obtained under condition (1), but significant increases in the water density at the gas/fluid channels were clearly observed (Fig. 2(a-2), (b-2) and Fig. S6(b), ESI†). These results indicate that the water-retention capacity of the MEA was already saturated at RH = 90% and further increasing the RH of the cathode gas to 100% caused liquid water to drain from the MEA to the gas/fluid channels outside of the GDLs. The high water density and low spatial occupancy (frequency) also suggested the drainage of liquid water in this region.

Operation of the PEFC under the condition (3) (under 20% O_2/N_2 flow with RH = 90%) led to a different trend of the water density, as shown in Fig. 2(a-3), (b-3) and Fig. S6(c) (ESI†). The water density at the interface between the cathode CL and GDL was greatly decreased, indicating the efficient drainage of the generated water from the cathode CL. By contrast, the maximum water density at the cathode gas/fluid channels outside of the cathode GDL was increased but the frequency was low. These findings suggest that the electrochemically generated water derived from the ORR in the cathode CL came into contact with the liquid water inside the cathode GDL and drained to the outside of the GDL.[32]

Although the drainage process of the generated water cannot be directly visualized by the current 3D imaging technique, the observed differences between the three sets of operating conditions at the cathode suggest that water produced by the ORR may enhance water drainage by contacting liquid water droplets in the GDLs. Mass transport simulations have been applied to elucidate the transient movement of water,[36] but realistic large-scale simulations still have difficulties in reproducing the characteristics of electrochemical operations and the complex structures inside PEFCs.[37] The current approach based on 3D X-ray CT imaging and statistical analysis has successfully clarified not only the differences in water distributions between each layer of the PEFC but also the significant changes in water drainage under PEFC power generation conditions for the first time.

Conclusions

In summary, we successfully visualized the 3D distribution of water in a commercial MEA with GDLs under PEFC operating conditions by in situ X-ray CT imaging. This technique provided valuable statistical data regarding the sample morphology, water density, and spatial occupancy of water in each layer of the MEA and GDLs. Increasing the humidity of N_2 supplied to the cathode did not markedly affect the amount and spatial occupancy of water in the MEA and GDLs, whereas performing the process under ORR conditions by supplying O_2 to the cathode significantly altered the water distribution, especially at the interface between the cathode CL and GDL. The proposed X-ray CT imaging technique represents a useful strategy for understanding water drainage in PEFCs under actual working conditions.

Author contributions

H. M. conceived the project and wrote the manuscript. T. O. carried out the electrochemical experiments and X-ray CT experiments. T. N. carried out the CT analysis and data statistical analysis. T. U. contributed to the setup of X-ray CT measurements. M. T. directed this study.

Conflicts of interest

The authors declare no conflicts of interest.

Acknowledgements

15118 | Phys. Chem. Chem. Phys., 2024, 26, 15115–15119

This journal is © the Owner Societies 2024

References

1 T. Lazaridis, B. M. Stühmeier, H. A. Gasteiger and H. A. El-Sayed, *Nat. Catal.*, 2022, **5**, 363.

2 R. Kumar and K. A. Subramanian, *Adv. Energy Res.*, 2022, **8**, 253.

3 F.-M. Du, T. A. Dao, P. V. J. Peitl, A. Bauer, K. Preuss, A. M. Bonastre, J. Sharman, G. Spikes, M. Perchthaler, T. J. Schmidt and A. Orfanidi, *J. Electrochem. Soc.*, 2020, **167**, 14.

4 P. Moçoteguy, B. Ludwig, D. Beretta and T. Pedersen, *Int. J. Hydrogen Energy*, 2020, **45**, 16724.

5 O. S. Ijaodola, Z. El-Hassan, E. Ogungbemi, F. N. Khatib, T. Wilberforce, J. Thompson and A. G. Olabi, *Energy*, 2019, **179**, 246.

6 G. Corda, S. Fontanesi and A. d'Adamo, *Int. J. Hydrogen Energy*, 2022, **47**, 14658.

7 H. Yumiya, M. Kizaki and H. Asai, *World Electr. Veh. J.*, 2015, **7**, 85.

8 K. Lim, C. Kim, R. Park, A. Alam and H. Ju, *Chem. Eng. J.*, 2023, **475**, 16.

9 P.-J. Lin, H.-Y. Wang, G.-D. Wang, J.-R. Li and J.-C. Sun, *Int. J. Hydrogen Energy*, 2022, **47**, 5541.

10 K. Nishida, Y. Kono, R. Funaoka and T. Furukawa, *J. Power Sources Adv.*, 2022, **16**, 6.

11 A. Syouji, M. Sakai, M. Hara and H. Matsushima, *Jpn. J. Appl. Phys.*, 2018, **57**, 5.

12 H. Nishiyama and J. Inukai, *ACS Omega*, 2023, **8**, 15318.

13 T. B. H. Tran, P. Huguet, A. Morin, M. Robitzer and S. Deabate, *J. Electrochem. Soc.*, 2022, **169**, 9.

14 K. Nishida, T. Hosotani and M. Asa, *Fuel Cells*, 2019, **19**, 60.

15 H.-C. Pei, C.-G. Xiao and Z.-K. Tu, *Appl. Energy*, 2022, **321**, 119349.

16 K. Ogawa, T. Sasaki, S. Yoneda, K. Tsujinaka and R. Asai, *J. Power Sources*, 2019, **444**, 227254.

17 H. Nishiyama, A. Iiyama and J. Inukai, *J. Power Sources Adv.*, 2022, **13**, 6.

18 Y. Aoyama, Y. Tabe, R. Nozaki, K. Suzuki, T. Chikahisa and T. Tanuma, *J. Electrochem. Soc.*, 2018, **165**, F484.

19 W. Yoshimune, Y. Higuchi, A. Kato, S. Hibi, S. Yamaguchi, Y. Matsumoto, H. Hayashida, H. Nozaki, T. Shinohara and S. Kato, *ACS Energy Lett.*, 2023, **8**, 3485.

20 P. Boillat, E. H. Lehmann, P. Trtik and M. Cochet, *Curr. Opin. Electrochem.*, 2017, **5**, 3.

21 H. Xu, S. Nagashima, H. P. Nguyen, K. Kishita, F. Marone, F. N. Büchi and J. Eller, *J. Power Sources*, 2021, **490**, 10.

22 P. Deevanhxay, T. Sasabe, S. Tsushima and S. Hirai, *J. Power Sources*, 2013, **230**, 38.

23 A. Kato, S. Kato, S. Yamaguchi, T. Suzuki and Y. Nagai, *J. Power Sources*, 2022, **521**, 11.

24 H. Matsui, N. Ishiguro, Y. Tan, N. Maejima, Y. Muramoto, T. Uruga, K. Higashi, D.-N. Nguyen, H.-C. Dam, G. Samjeské and M. Tada, *ChemNanoMat*, 2022, **8**, 7.

25 H. Matsui, K. Sato, N. Isobe, G. Samjeské, T. Uruga and M. Tada, *Catal. Sci. Technol.*, 2023, **13**, 4360.

26 J. Wu, L. G. A. Melo, X.-H. Zhu, M. M. West, V. Berejnov, D. Susac, J. Stumper and A. P. Hitchcock, *J. Power Sources*, 2018, **381**, 72.

27 K. Kinose, T. Suzuki, K. Kakinuma, M. Uchida, A. Iiyama and S. Tsushima, *ECS Trans.*, 2021, **104**, 185.

28 K. Nishida, T. Muranishi, Y. Ishizaki, S. Tsushima and S. Hirai, *ECS Trans.*, 2014, **64**, 853.

29 P. Deevanhxay, T. Sasabe, S. Tsushima and S. Hirai, *ECS Trans.*, 2013, **58**, 337.

30 R. F. Ziesche, J. Hack, L. Rasha, M. Maier, C. Tan, T. M. M. Heenan, H. Markötter, N. Kardjilov, I. Manke, W. Kockelmann, D. J. L. Brett and P. R. Shearing, *Nat. Commun.*, 2022, **13**, 11.

31 H. Xu, M. Bührer, F. Marone, T. J. Schmidt, F. N. Büchi and J. Eller, *J. Electrochem. Soc.*, 2022, **169**, 12.

32 Y. Nagai, J. Eller, T. Hatanaka, S. Yamaguchi, S. Kato, A. Kato, F. Marone, H. Xu and F. N. Büchi, *J. Power Sources*, 2019, **435**, 11.

33 T. Uruga, M. Tada, O. Sekizawa, Y. Takagi, T. Yokoyama and Y. Iwasawa, *Chem. Rec.*, 2019, **19**, 1444.

34 J. Miao, P. Ercius and S. J. L. Billinge, *Science*, 2016, **353**, 9.

35 H. Matsui, N. Ishiguro, T. Uruga, O. Sekizawa, K. Higashi, N. Maejima and M. Tada, *Angew. Chem., Int. Ed.*, 2017, **56**, 9371.

36 M. Nakauchi, T. Mabuchi, T. Hori, Y. Yoshimoto, I. Kinefuchi, H. Takeuchi and T. Tokumasu, *ECS Trans.*, 2017, **80**, 197.

37 T. Uenishi and R. Imoto, *J. Power Sources*, 2023, **573**, 10.

This journal is © the Owner Societies 2024

Phys. Chem. Chem. Phys., 2024, **26**, 15115–15119 | **15119**